RESEARCH ARTICLE

Plane Wave Reverse Time Image for Nondestructive Tests

WANQIU ZHENG[1], XIAOHONG MENG[1], AND JIAN WANG [2], (Member, IEEE)
[1]School of Geophysics and Information Technology, China University of Geosciences, Beijing, 100083, China
[2]Institute of Acoustics, Chinese Academy of Sciences, Beijing 100045, China

Corresponding author: Jian Wang (cugbwangjian@163.com)

ABSTRACT Reverse time migration (RTM) has been a popular method in industry duo to its ability of imaging complex subsurface and no dip restriction. However, RTM based on full matric capture (FMC) data is limited by the time cost of the calculation and cannot be widely used. In this study, a new strategy of RTM using a plane wave is proposed. Plane wave reverse time migration (PWRTM) does not need to stack the imaging results from multiple sources and directly uses the plane wave as a source function to reconstruct the image domain, reducing the influence of numerical dispersion in PWRTM. Low-rank finite difference (LRFD) is used in wavefield simulation, the core idea of LRFD is to use the quasi differential operator to compensate the error of time steps in conventional finite difference. Mathematical derivation proves that the algorithm can be considered as analytical in homogeneous background velocity. We use the LRFD method to drive the elastic PWRTM in nondestructive testing, and the vector decomposition method is used to ensure that the phase and amplitude characteristics of the P- and S-wave are not distorted. In our simulation, compared with the scalar imaging algorithm based on the Helmholtz method, the proposed imaging algorithm can more efficiently and accurately image large angle defects.

INDEX TERMS Reverse time migration (RTM), plane wave, nondestructive test, low-rank finite difference (LRFD).

I. INTRODUCTION

Reverse time migration (RTM) was developed by Whitemore [1], Basayl et al. [2], and McMechan [3] to image the seismic data. Duo to its ability of imaging complex subsurface and no dip restriction, RTM has been widely applied in medicine, industrial detection, and other fields. RTM is based on two-way wave equation [4], which can image complex velocity models. Theoretically, it can focus on any position in the image domain, and there is no inclination limit of crack comparing with any other methods. Multiple reflection and wave-mode conversion are also included in RTM naturally. For the detection of scattering points, plane wave imaging and delay stacking are good choices because of their fast calculation speed. However, this method is insufficient for imaging crack defects with different angles. For the multi-layer velocity model, conventional delay stacking and plane wave imaging require additional correction. The

calculation cost of these corrections is more than the imaging calculation itself.

RTM has been developed in the field of nondestructive testing (NDT) for several years. Fink [5] described the basic principles of ultrasonic time reversal. Lin et al. [6] applied pre-stack RTM to the scattered Lamb wave issue. To solve the emission problem, Saenger [7] used RTM to locate the emission source. Sabine Müller et al. [8] also showed the potential of RTM in NDT. Wilcox [9] described the method for finding the defects in the and showed good results. Park [10] adopted the time reversal method faced to the Lamb wave using circular piezoelectric transducers collocated on a thin plate. Sutin et al. [11] applied the RTM of the single-channel data in elastic solids.

In nondestructive testing, RTM is used as a technical method in various scenarios. However, a number of core problems remain to solve in the RTM itself, such as the imaging artifacts caused by backscattering, false frequency caused by insufficient data acquisition, simulation accuracy of high-frequency data, and wave-mode separation. In general, for

---

The associate editor coordinating the review of this manuscript and approving it for publication was Gongbo Zhou.

the wavefield with dominant frequency above 1 MHz, It is important to divide the smaller space grid and time sampling interval to obtain an accurate simulation using the finite difference method.

Whether in the field of geophysics, nondestructive testing, or medical imaging, the finite difference method is the basis of RTM. The principle of finite difference is simple, easy to implement, and suitable for GPU acceleration. However, the numerical dispersion caused by the finite difference has always troubled the users of RTM. To solve this problem, a finite difference algorithm based on low rank decomposition is proposed. This proposed method can provide accurate compensation in the direction of time derivative, particularly for the homogeneous isotropic background velocity. We applied this algorithm to solve the decoupled elastic wave equation [12]. The decoupled elastic wavefield did not need to separate the total wavefield after modeling and hold the phase and the anpliyude, and the P- and S-wave can be imaged directly without phase and amplitude changed. We used the plane wave function as the excitation source; thus, the plane wave data could be directly migrated in the imaging process, compared with the full matrix capture (FMC), the plane wave data required less storage and had a lower calculation cost. With the GPU acceleration algorithm, we can obtain high-efficiency and accurate linear fracture imaging results.

II. FINITE DIFFERENCE BASED ON LOW-RANK DECOMPOSITION

The finite difference algorithm is widely used in various fields because of its high efficiency. According to previous scholars' research, the wave field simulation method based on low rank decomposition is more accurate than the traditional finite difference algorithm [16]. In general, we used spatial and time differences to discretize the differential equation. The Lame equation describes the wave propagation in the homogeneous isotropic model.

$$\rho \frac{\partial^2 u}{\partial t^2} = (\mu + \lambda) \nabla (\nabla \cdot u) + \mu \nabla^2 u \qquad (1)$$

In equation 1, $u = (u_x, u_y, u_z)$ denotes the displacement component, μ and λ denote the Lame parameter, ρ is density, and ∇ denotes the derivative operator.

The Laplace operator can be expanded as follows:

$$\nabla^2 u = \nabla (\nabla \cdot u) - \nabla \times \nabla \times u \qquad (2)$$

If we describe equation 1 using v_p and v_s, We can derive equation 3, where $v_p = \sqrt{2\mu + \lambda}/\rho$ and $v_s = \sqrt{\mu}/\rho$.

$$\frac{\partial^2 u}{\partial t^2} = v_p^2 \nabla (\nabla \cdot u) + v_s^2 \nabla^2 u \qquad (3)$$

The above equation can be expanded to a second-order elastic wave equations, and its decoupled propagation form

is given by equation 4 [12].

$$\begin{cases} u(x,t) = u_p(x,t) + u_s(x,t) \\ w(x,t) = w_p(x,t) + w_s(x,t) \\ \dfrac{\partial^2 u_p(x,t)}{\partial t^2} = v_p^2 \left(\dfrac{\partial^2 u(x,t)}{\partial x^2} + \dfrac{\partial^2 w(x,t)}{\partial x \partial z} \right) \\ \dfrac{\partial^2 w_p(x,t)}{\partial t^2} = v_p^2 \left(\dfrac{\partial^2 u(x,t)}{\partial x \partial z} + \dfrac{\partial^2 w(x,t)}{\partial z^2} \right) \\ \dfrac{\partial^2 u_s(x,t)}{\partial t^2} = v_s^2 \left(\dfrac{\partial^2 u(x,t)}{\partial z^2} + \dfrac{\partial^2 w(x,t)}{\partial x \partial z} \right) \\ \dfrac{\partial^2 w_s(x,t)}{\partial t^2} = v_s^2 \left(\dfrac{\partial^2 w(x,t)}{\partial x^2} + \dfrac{\partial^2 u(x,t)}{\partial x \partial z} \right) \end{cases} \qquad (4)$$

In general, for spatial discretization, we use high order finite difference or other optimized operators to simulate wave propagation [13], [14]. However, for the discretization of time steps, we use the second-order discretization to represent the recurrence of the time direction. To compensate the numerical dispersion caused by finite difference. We define the quasi differential operator as equation 4.

$$Q[u(x)] = 2\pi^{-n} \int e^{i\xi \cdot x} q(x, \xi) u(\xi) d\xi \qquad (5)$$

In equation 4, Q denotes the quasi differential operator, $q(x, \xi)$ is the symbol of the quasi differential operator. $u(\xi)$ is an operator after the fast Fourier transform (FFT) of $u(x)$. n denotes the dimension.

When the main frequency of the source is extremely high, the finite difference method leads to the instability of the numerical solution owing to the large time sampling interval. To overcome this phenomenon, the spectral correction algorithm is used to modify the operator ik_x and ik_z using the symbol operator in the wavenumber domain. For constant background velocity, the compensation is accurate [15]. Based on symbolic theory, the quasi differential operator of the compensation term can be expressed as follows.

$$\begin{cases} Q_{x,j}^+ (\cdot) = F^{-1} \left\{ ik_x e^{+ik_x \cdot \frac{\Delta x}{2}} sinc \left(v_j(x) \Delta t \cdot \dfrac{k}{2} \right) F [\cdot] \right\} \\ Q_{x,j}^- (\cdot) = F^{-1} \left\{ ik_x e^{-ik_x \cdot \frac{\Delta x}{2}} sinc \left(v_j(x) \Delta t \cdot \dfrac{k}{2} \right) F [\cdot] \right\} \\ Q_{z,j}^+ (\cdot) = F^{-1} \left\{ ik_z e^{+ik_z \cdot \frac{\Delta z}{2}} sinc \left(v_j(x) \Delta t \cdot \dfrac{k}{2} \right) F [\cdot] \right\} \\ Q_{z,j}^- (\cdot) = F^{-1} \left\{ ik_z e^{-ik_z \cdot \frac{\Delta z}{2}} sinc \left(v_j(x) \Delta t \cdot \dfrac{k}{2} \right) F [\cdot] \right\} \end{cases} \qquad (6)$$

Equation 6 j denotes different wave modes (v_p and v_s). If we use the symbolic operator to compensate the time discreteness directly, the computational cost is $O(N_x log N_x)$, and N_x is the sample number. To reduce the computational cost, Fomel et al. [16] developed a so-called Low-rank method in hybrid domain. To reduce the computational complexity, this study used the hybrid domain low rank decomposition algorithm. For $M_{s,x} = k_x sinc(*)$, the low rank decomposition form can be written as:

$$M_{s,x} = \sum_{i=1}^{I} \sum_{j=1}^{J} m_{s,x}(x, k_m) \cdot r_{m*n} \cdot m_{s,x}(x_n, k) \qquad (7)$$

where $m_{s,x}(x, k_m)$ and $m_{s,x}(x_n, k)$ are the submatrix of $M_{s,x}$ with m columns and n rows.

Quasi differential operator Q in equation 6 can also be given using the low rank method. It is clear that $m_{s,x}(x, k_m)$ only concerns the wavenumber; thus, we can derive equation 8.

$$m_{s,x}(x_n, k) \approx \sum_{h=1}^{N} C_{s,x}(x_n, h) \cdot B(h, k) \qquad (8)$$

In equation 8, $B(h, k)$ denotes a matrix of $h \times k$, h is the finite difference order, and k is the sample number in wavenumber. It can be calculated by $\sin\left((2h - 1) \cdot k \cdot \frac{\Delta x}{2}\right)$.

Here, we can define a new equation using the low rank form:

$$O_{s,x}(x, h) = \sum_{i=1}^{I} \sum_{j=1}^{J} m_{s,x}(x, k_m) \cdot r_{m*n} \cdot C_{s,x}(x_n, h) \qquad (9)$$

Based on equation 9, quasi differential operator Q can be written as equation 10.

$$Q_{x,s}^{+}(u) \approx \frac{1}{2} \sum_{h=1}^{N} (x, h) F^{-1}$$
$$\times \left\{ \left(e^{ik_x \cdot \Delta x \cdot l} - e^{ik_x \cdot \Delta x \cdot (l-1)} \right) \cdot F[u] \right\} O_{s,x} \qquad (10)$$

Using the FFT translation property, the above equation can be written as equation 11, which is the final form of the low rank finite difference operator.

$$Q_{x,s}^{+}(u) \approx \frac{1}{2} \sum_{h=1}^{N} O_{s,x}(x, h) \left\{ u(x_{right}, t) - u(x_{left}, t) \right\} \qquad (11)$$

In equation 11, $x_{right} = (x + h \times \Delta x, y)$, $x_{left} = (x - (h - 1) \times \Delta x, y)$, and h is the finite difference order. $Q_{x,j}^{-}(\cdot)$, $Q_{z,j}^{+}(\cdot)$, and $Q_{z,j}^{-}(\cdot)$ also have the same form.

III. SIMULATION OF ELASTIC WAVE AND DECOMPOSITION

For elastic RTM, the conversion of the multi wave-mode can affect the imaging work, and imaging of the uncorrelated wave-mode introduces imaging artifacts. The conventional Helmholtz method can separate the P- and S-wave in the scalar field efficiently, but it changes the phase and amplitude of the waveform. The Poynting method is also an efficient procedure, however, it cannot handle the overleap events. For small-scale inverse scattering problems, the change of phase and amplitude adds difficulties to the location of scattering source. In this study, the low rank decomposition algorithm was used to solve the second-order elastic wave decoupled equation. The advantage of this algorithm is that it ensures the stability of the calculation. Moreover, the vector P- and S-wave with accurate phase and amplitude can be obtained without the additional derivation calculation.

To prove the effectiveness of the decoupled equation, we performed a numerical simulation and compared the decoupled propagation operator with the Helmholtz decomposition. In this test, the Ricker wavelet with the center frequency of 5 MHz was excited in the center of the model.
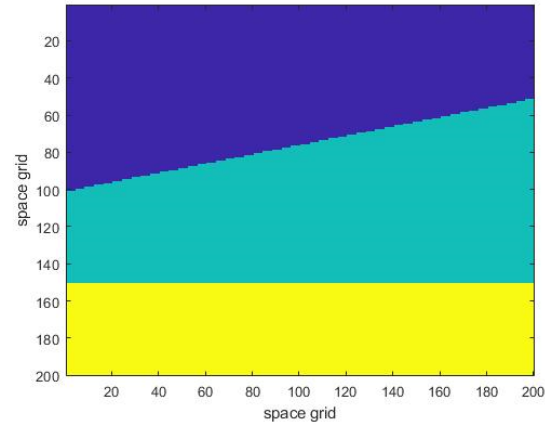

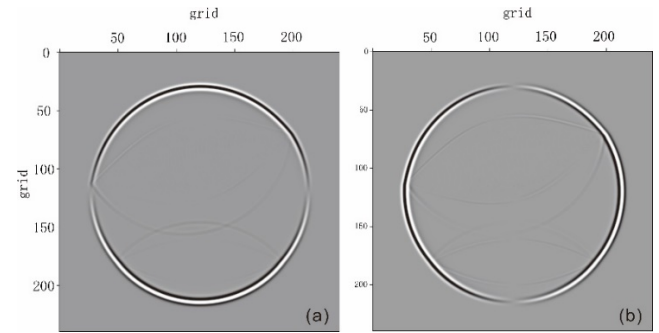**FIGURE 1.** P-velocity model with three layers.

FIGURE 2. Original wavefield: (a) Elastic x-component; (b) Elastic z-component.

The mesh size of the model space is 400×400, and the spatial samping is 0.6mm, time samping is 1ms, and Figure 1 shows the P-velocity model. The S-velocity is written as $v_p = \sqrt{3}v_s$, and we used constant density. The P-velocity model includes three layers with a velocity change from 2100 to 2,300 m/s. Figure 2 shows the original wavefields with the x- and z-component. In original wavefields, it is difficult to distinguish the P- and S-waves. Figure 3 shows the decoupled propagation wavefields. In this case, we can obtain the vector P- and S-wavefields. Figure 4 shows the scaler P- and S-wavefields calculated by the Helmholtz method. To compare the phase and amplitude, we show the waveform in Figures 5 and 6. We can clearly see that the P- and S-wave calculated by the Helmholtz method not only destroy the vector information of the original wavefield, but also affect the amplitude and phase of the waveform. The wavefield separation based on decoupled operator preserves the phase and amplitude information of the original P- and S-wave well and does not damage the structure of the vector, this decoupled equations give better separation results. The Helmholtz decomposition for separating the P- and S-wave causes the phase rotation for the S-wave. An additional method is required to correct the phenomenon, And it also requires additional time costs, such as the use of Hilbert transform.

IV. PLANE WAVE REVERSE TIME MIGRATION

In general, we used the wavenumber domain imaging method, which was the fastest for plane wave data. This
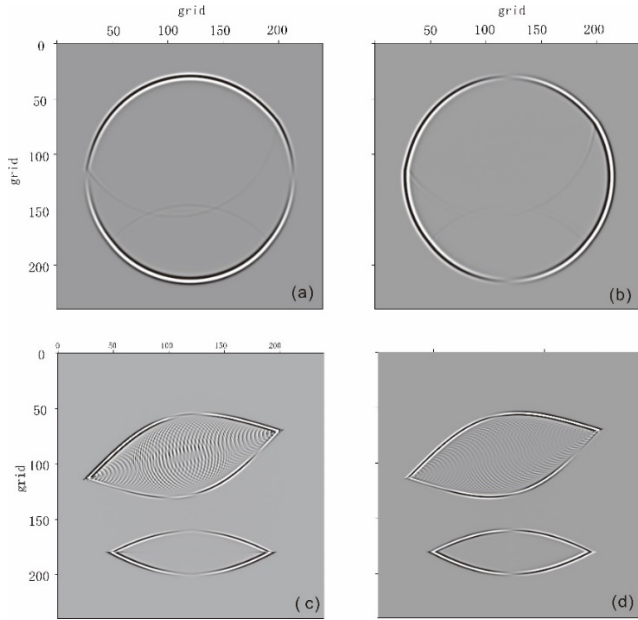
FIGURE 3. Decoupled propagation operator. (a) P-wave x-component; (b) P-wave z-component; (c) S-wave x-component; (d) S-wave z-component.
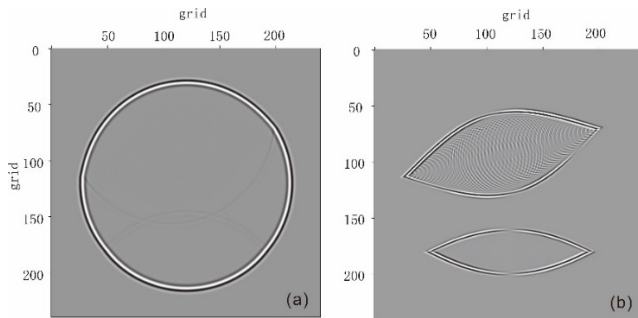

FIGURE 4. Helmholtz method. (a) Scaler P-wavefield; (b) Scaler S-wavefield.
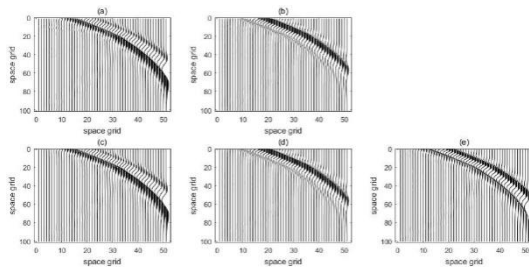

FIGURE 5. P-waveform calculated by the decoupled operator and Helmholtz method. (a) Original wavefield x-component; (b) original wavefield z-component; (c) P-wave x-component using decoupled operator; (d) P-wave z-component using decoupled operator; (e) P-wave using the Helmholtz method.

FIGURE 6. S-waveform calculated using the decoupled operator and Helmholtz method. (a) Original wavefield x-component; (b) original wavefield z-component; (c) S-wave x-component using decoupled operator; (d) S-wave z-component using decoupled operator; (e) S-wave using the Helmholtz method.

FIGURE 7. Workflow of plane wave reverse time migration (PWRTM).

cross-correlates with the received field at the same time of reverse time propagation and finally obtains the imaging result. It is different from RTM based on FMC data, because PWRTM has less loops between different sources. Figure 7 shows the PWRTM workflow.

The imaging condition is the most important core technology of RTM or PWRTM. A cross-correlation imaging condition is typically used in RTM, but for the decoupled propagator, the inner product imaging condition can obtain a more accurate imaging effect.

$$I_{i,j}(x,z) = \frac{\sum_t \vec{S}[t,x,z,i] \cdot \vec{R}[t,x,z,j]}{\sum_t \left\| \vec{S}[t,x,z,i] \right\|^2} \tag{12}$$

which is similar to the cross-correlation imaging conditions. The new imaging condition is also normalized by the source wavefield, the so-called normalized source illumination. In equation 12, $\vec{S}$ denotes the vector source wavefields, $\vec{R}$ denotes the vector received wavefields, and i and j denote P-wave model and S-wave model.

In this study, we showed different wave-modes of the PWRTM results using inner product and cross-correlation imaging conditions. The ways we compared in this study are listed below:

(1) Vector P-P image using the inner product imaging condition

(2) Vector S-S image using the inner product imaging condition

algorithm is efficient and can realize real-time imaging in the NDT field. However, for certain linear defects with different angles, the wavenumber domain algorithm cannot accurately work. The destructive behavior caused by linear defects is often highly dangerous. To address this problem, the plane wave reverse time migration (PWRTM) can complete the imaging work.

The PWRTM sets the plane wave as the excitation source; the source generates the forward propagation and
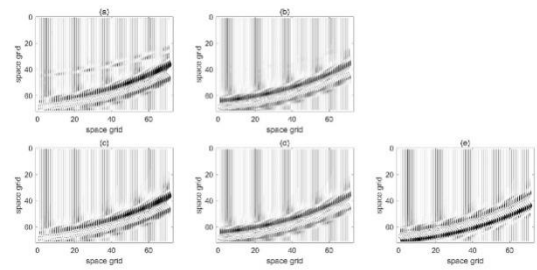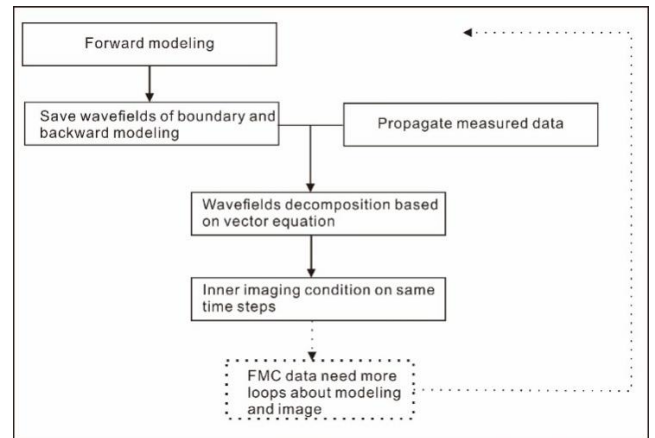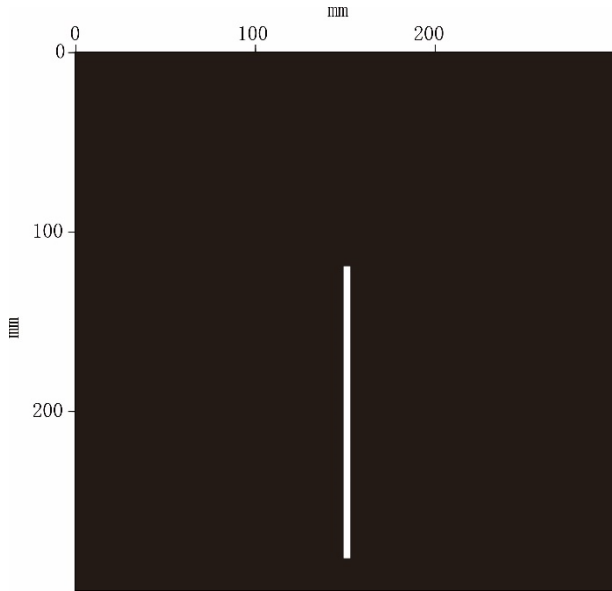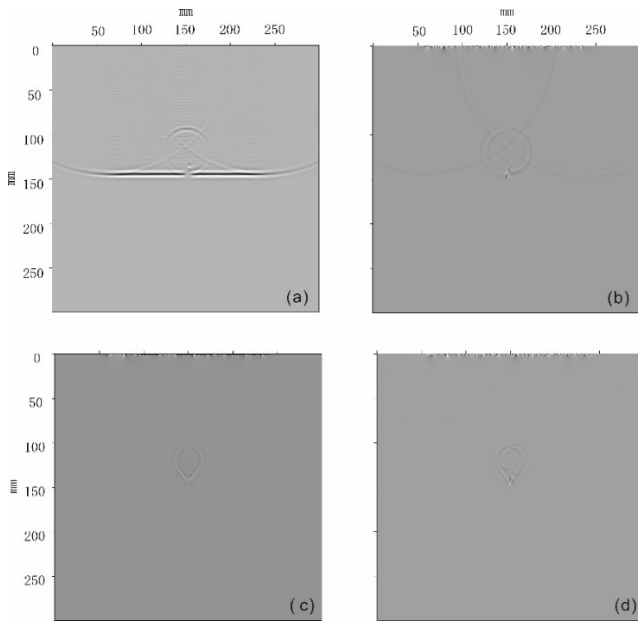
FIGURE 8. P-velocity model.

FIGURE 9. Forward modeling in vector PWRTM; (a) P-wave z-component; (b) P-wave x-component; (c) S-wave z-component; (d) S-wave x-component.
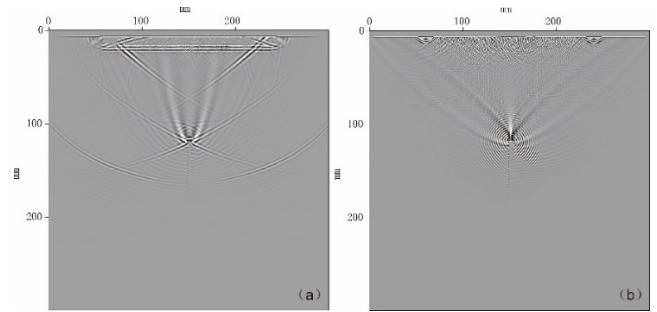

FIGURE 10. Scaler PWRTM using the Helmholtz method. (a) P-P wave model image; (b) S-S wave model image.
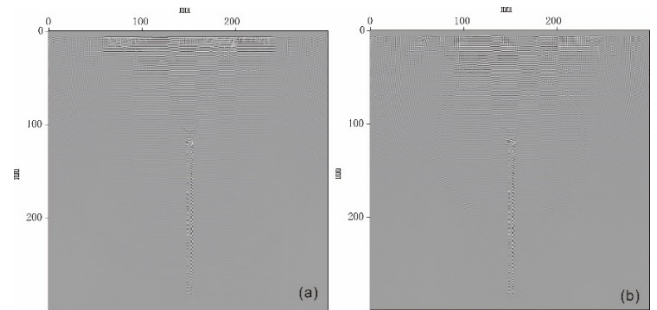

FIGURE 11. Vector PWRTM using the decoupled operator. (a) P-P wave mode image; (b) S-S wave mode image.
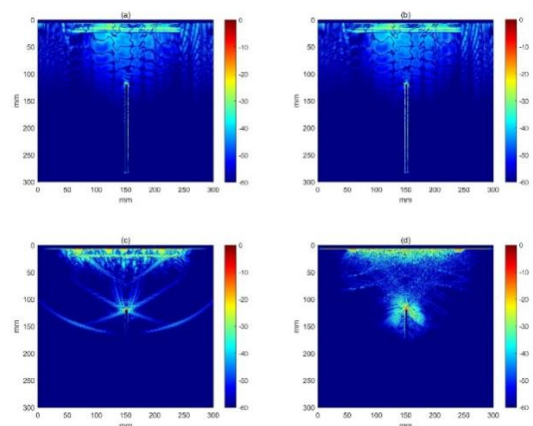

FIGURE 12. PWRTM results within 0–60 dB. (a) P-P wave mode image using decoupled operator; (b) S-S wave mode image using decoupled operator; (c) P-P wave mode image using the Helmholtz method; (d) S-S wave mode image using the Helmholtz method.

(3) Scaler P-P image using cross-correlation imaging conditions

(4) Scaler S-S image using cross-correlation imaging conditions

In this simulation, the main frequency of the excitation source is 5 MHz, the discrete grid point is 500 * 500 with a spatial samping of 0.6mm. The velocity model is shown in Figure 8, and the background P-velocity was 6000 m/s. The S-velocity is written as $v_p = \sqrt{3}v_s$, and we used a constant density. The defect was located in the middle of the velocity model and perpendicular to the front of the plane wave. The linear array element was located at the center of the model surface, and a total of 200 excitation sources were emitted at

the same time. The front of the wave formed by the linear array element is a plane wave, as shown in Figure 9. Figure 9 shows the wave-mode decomposition in the imaging process. When the single-component vertical excitation source passes through the scattering point, the waveform conversion occurs. The decoupled operator can ensure the separation of wave modes without losing vector information.

We used random boundary conditions to ensure the accuracy of wavefield back propagation and retain the total energy of the wavefield. Figure 10 shows the scalar imaging results obtained by the Helmholtz method and cross-correlation imaging condition. Because the Helmholtz method requires more derivative calculation and changes the phase and amplitude information of the original wavefield, it is not difficult to find from the imaging results that although the position of

the vertical defect can be located by this method, the imaging quality is satisfactory. Figure 11 shows the vector imaging results based on the decoupled operator and inner product imaging condition. Figure 12 shows the dynamic range of imaging results from 0 to 60 dB. The decoupled propagator can protect waveform and vector information without significantly increasing computation under the same conditions. From the imaging results of this method, we can clearly see that the defect description of the proposed algorithm was significant. Compared with the scalar imaging algorithm, the proposed imaging algorithm has an overwhelming advantage. The proposed algorithm was accelerated by GPU high-performance equipment, the calculation time of the imaging process was 4.223 seconds, and the scaler imaging process was 3.748 seconds.

V. CONCLUSION

For the imaging problem caused by linear defects, a plane wave reverse time migration algorithm based on the decoupled wave equation is proposed. In this proposed algorithm, the decoupled operator is used to retain the amplitude and phase information of different wave modes, and the low rank decomposition is used to ensure the accuracy of wave propagation. We compared the imaging results based on the vector wavefield with those based on the scalar wavefield and proved that the image based on vector decomposition was more accurate in detailed descriptions. Compared with the reverse time migration algorithm based on FMC data, the proposed algorithm requires less computation, because it needs no loop between different source wavefields, In summary, the transform domain method [17] and reverse time migration [16] algorithm have great potential for application in non-destructive testing.

REFERENCES

[1] N. D. Whitmore, "Iterative depth migration by backward time propagation," in *Proc. 53rd Annu. Int. Meeting SEG, Expanded Abstr.*, 1983, pp. 382–385.

[2] E. Baysal, D. D. Kosloff, and J. W. C. Sherwood, "Reverse time migration," *Geophysics*, vol. 48, pp. 1514–1524, Nov. 1983.

[3] G. A. McMechan, "Migration by extrapolation of time-dependent boundary values," *Geophys. Prospecting*, vol. 31, no. 3, pp. 413–420, Jun. 1983.

[4] J. Etgen, S. H. Gray, and Y. Zhang, "An overview of depth imaging in exploration geophysics," *Geophysics*, vol. 74, no. 6, pp. WCA5–WCA17, Nov. 2009.

[5] M. Fink, "Time reversal of ultrasonic fields. I. Basic principles," *IEEE Trans. Ultrason., Ferroelectr., Freq. Control*, vol. 39, no. 5, pp. 555–566, Sep. 1992.

[6] X. Lin and F. G. Yuan, "Prestack reverse-time migration in structural health monitoring," in *Proc. 41st Struct., Struct. Dyn., Mater. Conf. Exhibit*, 2000.

[7] E. H. Saenger, "Time reverse characterization of sources in heterogeneous media," *NDT E Int.*, vol. 44, no. 8, pp. 751–759, Dec. 2011.

[8] S. Müller, E. Niederleithinger, and T. Bohlen, "Reverse time migration: A seismic imaging technique applied to synthetic ultrasonic data," *Int. J. Geophys.*, vol. 2012, Jul. 2012, Art. no. 128465.

[9] P. D. Wilcox, "A rapid signal processing technique to remove the effect of dispersion from guided wave signals," *IEEE Trans. Ultrason., Ferroelectr., Freq. Control*, vol. 50, no. 4, pp. 419–427, Apr. 2003, doi: 10.1109/tuffc.2003.1197965.

[10] H. W. Park, "Numerical simulation and investigation of the spatial focusing of time reversal A_0 Lamb wave mode using circular piezoelectric transducers collocated on a rectangular plate," *J. Sound Vibrat.*, vol. 332, no. 11, pp. 2672–2687, May 2013.

[11] A. M. Sutin, J. A. TenCate, and P. A. Johnson, "Single-channel time reversal in elastic solids," *J. Acoust. Soc. Amer.*, vol. 116, no. 5, pp. 2779–2784, Nov. 2004.

[12] W. Wang, G. A. McMechan, C. Tang, and F. Xie, "Up/down and P/S decompositions of elastic wavefields using complex seismic traces with applications to calculating Poynting vectors and angle-domain common-image gathers from reverse time migrations," *Geophysics*, vol. 81, no. 4, pp. S181–S194, Jul. 2016.

[13] J.-H. Zhang and Z.-X. Yao, "Optimized finite-difference operator for broadband seismic wave modeling," *Geophysics*, vol. 78, no. 1, pp. A13–A18, Jan. 2013.

[14] Y. Liu and M. K. Sen, "An implicit staggered-grid finite-difference method for seismic modelling," *Geophys. J. Int.*, vol. 179, no. 1, pp. 459–474, Oct. 2009.

[15] K. Firouzi, B. T. Cox, B. E. Treeby, and N. Saffari, "A first-order k-space model for elastic wave propagation in heterogeneous media," *J. Acoust. Soc. Am.*, vol. 132, no. 3, pp. 1271–1283, 2012.

[16] S. Fomel, L. Ying, and X. Song, "Seismic wave extrapolation using lowrank symbol approximation," *Geophys. Prospecting*, vol. 61, no. 3, pp. 526–536, May 2013.

[17] H. Chen, H. Zhou, Q. Zhang, and Y. Chen, "Modeling elastic wave propagation using k-space operator-based temporal high-order staggered-grid finite-difference method," *IEEE Trans. Geosci. Remote Sens.*, vol. 55, no. 2, pp. 801–815, Feb. 2017.

WANQIU ZHENG received the bachelor's and master's degrees in geophysics from the China University of Geosciences, Beijing, China, in 2014 and 2017, respectively, where she is currently pursuing the Ph.D. degree.

XIAOHONG MENG received the Ph.D. degree in geophysics from the China University of Geosciences, Beijing, China, in 1991. She is currently a Professor with the School of Geophysics and Information Technology, China University of Geosciences. Her research interests include processing and interpretation of gravity and magnetic data.

JIAN WANG (Member, IEEE) received the bachelor's degree in geophysics from the China University of Geosciences, Beijing, China, in 2014, and the Ph.D. degree, in 2018. He did postdoctoral research work with the Institute of Geology and Geophysics, Chinese Academy of Sciences, Beijing, where he is currently an Assistant Researcher with the Institute of Acoustics.

• • •